Author/s:
Rose, JJA;Johnson, MD;Reyhani, M;Batinovic, S;Seviour, RJ;Ghosal, D;Petrovski, S

Title:
Mutations in Gordonia amarae mycolic acid biosynthetic pathway confer resistance to Patescibacteria parasite Mycosynbacter amalyticus

Date:
2025

Citation:
Rose, J. J. A., Johnson, M. D., Reyhani, M., Batinovic, S., Seviour, R. J., Ghosal, D. & Petrovski, S. (2025). Mutations in Gordonia amarae mycolic acid biosynthetic pathway confer resistance to Patescibacteria parasite Mycosynbacter amalyticus. Nature Communications, 16 (1), https://doi.org/10.1038/s41467-025-56933-4.

Persistent Link:
https://hdl.handle.net/11343/360129

nature communications

Article

https://doi.org/10.1038/s41467-025-56933-4

Mutations in *Gordonia amarae* mycolic acid biosynthetic pathway confer resistance to Patescibacteria parasite Mycosynbacter amalyticus

Received: 9 October 2024

Accepted: 5 February 2025

Published online: 05 March 2025

Check for updates

Jayson J. A. Rose[1,2], Matthew D. Johnson[3,4], Milad Reyhani[3,4], Steven Batinovic[1], Robert J. Seviour[1], Debnath Ghosal[3,4,5] ✉ & Steve Petrovski[1,2,5] ✉

The obligate necrotrophic parasite, *Candidatus* Mycosynbacter amalyticus, a member of the Patescibacteria has been isolated from wastewater. Subsequent efforts have been directed toward unravelling its biological lifecycle and attachment mechanism facilitating infection and subsequent lysis of its *Actinobacterial* host, *Gordonia amarae*. Here, using electron cryo-tomography (CryoET), we reveal the molecular anatomy of parasitic Mycosynbacter amalyticus cells, uncovering an unusual infection process. Through laboratory-based evolution experiments, we generated eleven slow-growing independent spontaneous *Gordonia amarae* resistant mutants. Mycolic acids (MA) are key components of the outer cellular envelope of *G. amarae* and other *Actinobacteria*, with MA being the physical attribute implicated in *G. amarae* associated wastewater foaming. CryoET and genome sequencing exposed absence of intact MA and an associated suite of mutations predominantly occurring within the *pks13* and *pptT* genes of the MA biosynthetic pathway. Our findings suggest that MA structural integrity is critical for attachment of *Ca*. Mycosynbacter amalyticus to its host.

Wastewater treatment is a global process using complex microbial communities to degrade potential environmentally harmful substrates to products with relatively little environmental impact[1,2]. While next generation DNA sequencing has allowed us to identify members of these communities, how they interact with each other is largely unknown. Members of the Patescibacteria are one example and are routinely detected through metagenomic analysis[3–5]. This phylum forms a substantial component of the difficult-to-culture, enigmatic microorganisms referred to as 'microbial dark matter', because of their frequent detection yet unknown function[6]. Until recently, little was known about the Patescibacteria, but several populations have now been isolated from a variety of environments other than wastewater treatment plants (WWTPs). These include the human oral microbiome[7] and insects[8], with all isolates characterised as obligate parasites of their actinobacterial hosts. The hosts of these organisms presumably provide essential materials that are unable to be synthesised de novo by these parasites due to their highly reduced genome sizes[9].

[1]Department of Microbiology, Anatomy, Physiology and Pharmacology, La Trobe University, Bundoora, VIC, Australia. [2]La Trobe Institute for Molecular Sciences (LIMS), La Trobe University, Bundoora, VIC, Australia. [3]Department of Biochemistry and Pharmacology, Bio21 Molecular Science and Biotechnology Institute, The University of Melbourne, Melbourne, VIC, Australia. [4]ARC Centre for Cryo-electron Microscopy of Membrane Proteins, Bio21 Molecular Science and Biotechnology Institute, University of Melbourne, Parkville, VIC, Australia. [5]These authors contributed equally: Debnath Ghosal, Steve Petrovski. ✉e-mail: debnath.ghosal@unimelb.edu.au; steve.petrovski@latrobe.edu.au

Candidatus Mycosynbacter amalyticus strain JR1[10], henceforth referred to as M. amalyticus, emerged unexpectedly during attempts to isolate bacteriophages lytic against the foam stabilising bacterium *Gordonia amarae*. This obligate parasite was then the first member of the Patescibacteria to be cultivated outside the human oral microbiome[11,12]. Its ultra-small size and unique lifecycle have increased the challenge of understanding key features of its parasitic behaviour, including how it is attracted towards its host cell and whether the method/s used for subsequent cell lysis are physical or chemical[5,7–9,13,14]. Earlier low-resolution transmission electron microscopy studies with other Patescibacterial obligate parasites have generated equivocal information[7,10].

Here, we used electron cryo-tomography (cryoET) to investigate how M. amalyticus interacts with the *G. amarae* cell surface during and after cell-to-cell contact. To further explore and clarify this relationship, we also generated several *Gordonia amarae* mutants (GAMs), all of which were resistant to M. amalyticus infection. Through whole genome sequencing (WGS), these mutations were consistently identified in genes responsible for the synthesis of the outer mycolic acid (MA) membrane, suggesting that it is this structure which facilitates attraction, attachment and eventual host cell penetration by M. amalyticus.

Results

CryoET of M. amalyticus and *G. amarae* depict intimate cell surface interaction, and unique ultrastructures

Electron cryo-tomography (cryoET) allows us to visualise intercellular interactions at nanometre resolution[15–17]. We used cryoET to investigate interactions between M. amalyticus and its prey *G. amarae*. Host cells were incubated with M. amalyticus and vitrified on Quantifoil holey carbon grids. Similar to previous negative staining observations[10], low-resolution projection images (Supplementary Fig. 1) captured multiple M. amalyticus cells forming close interactions with their prey. *G. amarae* is Gram-positive bacterium with a thick peptidoglycan wall and dense outer MA membrane, presenting with a "mere pounamu" (one pole is wider than the other) cellular morphology. To capture high-resolution visualisation, we needed to overcome the technical obstacles that these inherent cellular features pose, requiring us to target interactions occurring at the narrow end of *G. amarae* cells. Our cryo-tomogram in Fig. 1a displays a M. amalyticus cell forming a tight interaction with its *G. amarae* prey, providing clear resolution of the cytoplasmic and MA membranes of *G. amarae*, as well as the cytoplasmic membrane and diffused outer cell wall of M. amalyticus. Closer inspection and 3D segmentation of the interaction site revealed two distinct features: (i) multiple thin filaments extending

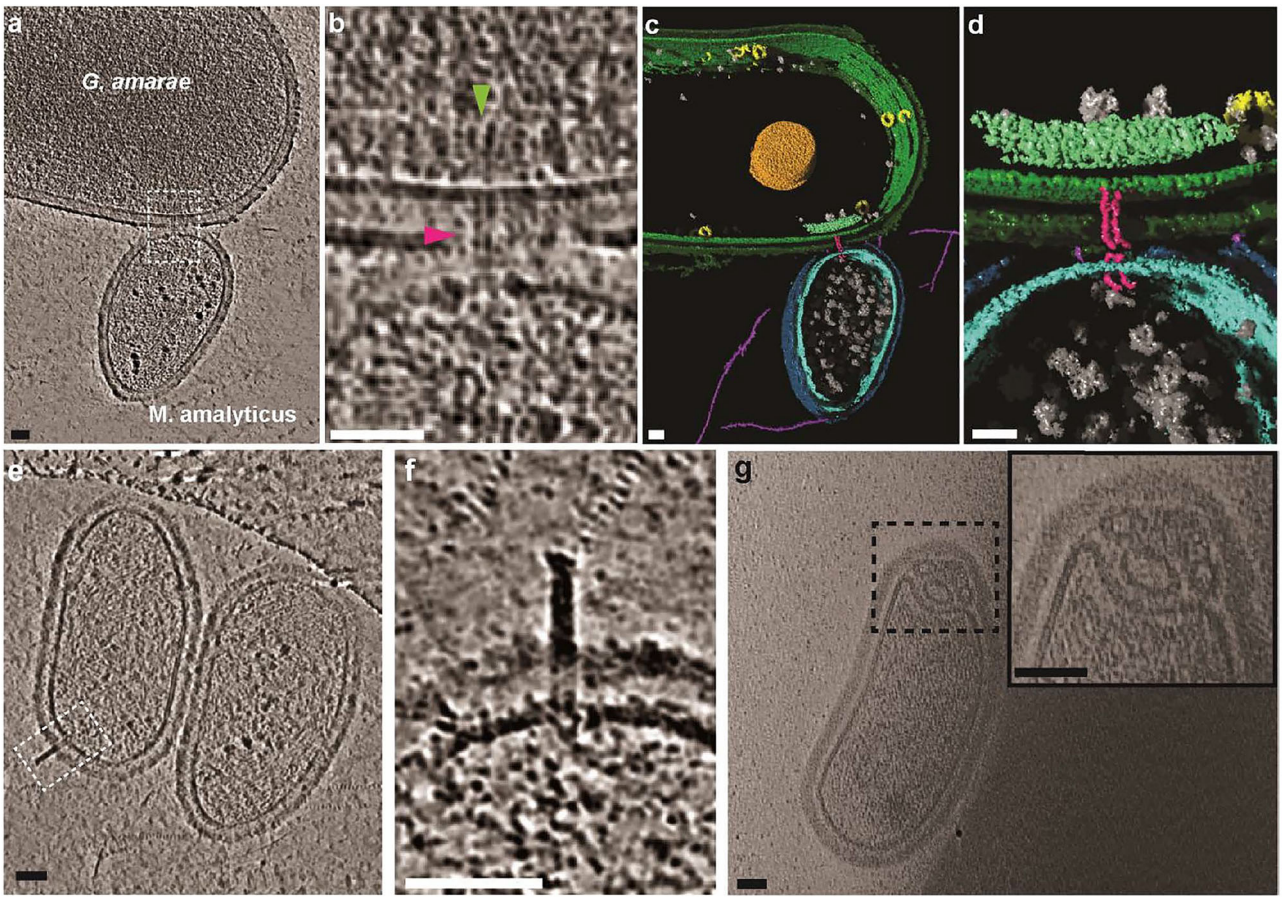

Fig. 1 | The anatomy of M. amalyticus predation of *G. amarae*. **a** Example tomogram of *G. amarae* CON44^T and M. amalyticus interaction, images are 2D slices through a 3D tomogram (weighted back projection, TomoSim filtered, thickness = 10). M. amalyticus cell (~300–500 nm in length) can be seen forming a tight interaction with *G. amarae* CON44^T cell (~500–1000 nm in width). **b** A closer view of the interaction reveals a tube density forming between the two cells (pink arrow head), and protein array forming within *G. amarae* (green arrow head). **c**, **d** Segmented 3D volumes of tomograms shown in (**a**, **b**) (pili = purple; lance/tube structure = pink; *G. amarae* cytoplasmic membrane = green; cytoplasmic vesicles = yellow; storage granule = orange; M. amalyticus JR1 outer layer = dark blue; M. amalyticus cytoplasmic membrane = teal). **e** Example tomograms of M. amalyticus JR1, images are 2D slices (thickness = 10) through 3D reconstructed tomogram. Cell membranes, type 4 pili and a lance-like structure are clearly visible. **f** Closer view of the lance structure protruding from the M. amalyticus cell, parallel lines through the cell envelope of M. amalyticus are indicative of a lance/tube structure. **g** Cellular compartments present at the poles of predatory M. amalyticus cells during attachment to a *G. amarae* cell, closer view shown in the inset. All scale bars represent 50 nm (See supplementary movie 1 for more detail).

from M. amalyticus cells and anchoring to the surface of *G. amarae* (Fig. 1c purple); (ii) and a tube-like conduit traversing the two cell types (Fig. 1b, d pink). The thin filaments extending from M. amalyticus cells are likely type IV pili, as indicated earlier by pilin gene annotation within the M. amalyticus genome sequence[10]. Moreover, the dimensions of these filaments (6.1 nm, ±0.62 nm width) are consistent with previously reported type IV pili dimensions[18]. When focusing on the tube-like conduit, measurements from our reconstructed tomograms indicate that the tube is approximately 8.6 nm ± 0.7 nm wide and 61 nm long. To assist with structure recognition, 3D segmentation of cryotomograms highlighted additional features proximal to the interaction and along the *G. amarae* cell periphery (see Supp movie 1). Inside the *G. amarae* cytoplasm, we observed an ordered protein array (Fig. 1c, d, green) adjacent to this conduit, several cytoplasmic vesicles and a storage granule (Fig. 1c, d, yellow and orange respectively). Reconstructed tomograms of M. amalyticus cells incubated with either *G. amarae* or spent media from a *G. amarae* culture, periodically had lance-like structures protruding from their cell poles (Fig. 1e, f). These lances comprise a tube-like structure extending 70 nm ± 4 nm from the inner membrane of the M. amalyticus cell to the extracellular milieu with a barb density positioned at the tip (Fig. 1f). These lance-like structures were observed intermittently, with only 15 found in 33 tomograms examined, but were absent in M. amalyticus cells that had no recent interaction with *G. amarae*. The tube component of the lance-like structures was similar in dimension to the tube-like conduit observed in the *G. amarae* – M. amalyticus interaction (lance diameter 8.98 nm ± 0.58). Unexpectedly, complex cellular "compartments" were also frequently present (54% of captured data) at the poles of M. amalyticus cells attached to *G. amarae* (Fig. 1g). These compartments were not observed in M. amalyticus monocultures and only in the presence of its host. Our results suggest a mechanism whereby M. amalyticus uses multiple nanostructures, only observed during infection of *G. amarae* that facilitate lytic parasitism. Their individual functions are unknown thus far.

Generation of slow growing *Gordonia amarae* mutants (GAMs) that are resistant to M. amalyticus infection

By repeating the batch experiments performed previously[10], a spontaneous *G. amarae* CON44^T mutant resistant to M. amalyticus lysis was generated, and named *Gordonia amarae* mutant 1 (GAM1). The observed recovery in population growth prompted isolation and purification of the survivors. This experimental approach provided a blueprint to isolate more independently generated *Gordonia amarae* mutants (GAMs), yielding ten additional mutants. These mutants exhibited slow growth compared to the wild type *G. amarae* (Fig. 2a, Supplementary Fig. 2a). We next compared the growth rate of each GAM to the wild type *G. amarae* in liquid culture, and then challenged with M. amalyticus in liquid coculture. In contrast to the substantial reduction of wild type *G. amarae* growth in M. amalyticus coculture, M. amalyticus had no impact on the growth rate of the GAMs (Fig. 2a, Supplementary Fig. 2a). We then measured the replication of M. amalyticus utilising direct digital-PCR (dPCR), which confirmed that M. amalyticus could only replicate in coculture with *G. amarae* CON44^T (Fig. 2b). The unimpeded growth of each GAM, and lack of M. amalyticus replication suggested a loss of interaction between the host and parasitic organisms.

To provide real-time visualisation of surface interaction between GAMs and M. amalyticus, we then employed live cell fluorescence microscopy. Interestingly, *G. amarae* readily incorporated the membrane dye, staining cells green, however the GAMs were more reluctant to assimilate the membrane dye. Imaging showed that M. amalyticus rapidly associated with wild type *G. amarae*, maintaining surface contact with its host as expected (Fig. 2c, Supplementary movie 2). In contrast, M. amalyticus was unable to maintain surface attachment with the GAMs, with short lived, or little to no co-localisation of cells (Fig. 2d, Supplementary movie 3). Furthermore, GAM cellular shape and configuration of filament morphology had also changed, now appearing rigid and withered, lacking cell shape uniformity in comparison to *G. amarae* CON44^T (Supplementary Fig. 2b, c).

Genome sequence of GAMs reveal mutations within the mycolic acid biosynthetic pathway

In the eleven spontaneous mutants generated, all mutations occurred in five different loci as either single nucleotide polymorphisms (SNPs) or small deletions (Table 1, Supplementary data 1). Among these five loci, GAM6, GAM7, GAM10, GAM11 and GAM12 all possessed a mutation within the first locus, occurring in different locations within the *pks13* gene, encoding a large multifunctional polyketide synthase (condensase), responsible for the final condensation of MA[19,20]. The exception was GAM12, where the mutation was located in the predicted a*ftB* gene (Fig. 3a), encoding a protein involved in the 'endpoint' for arabinogalactan (AG) arabinan biosynthesis[21]. AG is critical for the incorporation of MA into the cell wall, providing an anchor for the attachment of MA[22,23], linking this structure to the underlying peptidoglycan[24]. In the site-specific mutations of *pks13*, the impacted catalytic domains were uncovered (Fig. 3b). Based on sequence alignments with *Mycobacterium tuberculosis* strain H37Rv (Mtb), SNPs in GAM7, GAM10 and GAM11 resulted in missense mutations and an in-frame deletion in GAM6, with each likely impacting the predicted active sites of Pks13 and resulting in loss of function. The translated sequence of the *G. amarae pks13* gene shares a 49.5% total identity with Mtb, containing a high level of conservation across the catalytic domains (Fig. 3c). Mutations identified in the *pks13* gene were all located in two of five domains, the predicted active site of the keto-synthase (KS) domain of GAM10, and within the thio-esterase (TE) domain of GAM6, GAM7 and GAM11 (Table 1 and Fig. 3b, c).

Mutations occurring in GAM1, GAM4 and GAM9 were all within the predicted *pptT* gene identified in the second locus (Table 1 and Fig. 3d), encoding a 4' - phosphopantetheinyl transferase (PPTase), involved in the activation of Pks13 through posttranslational modification (Fig. 3b)[25]. Loss of PptT activity abolishes MA synthesis, proving lethal in *M. tuberculosis* complex although tolerable in other Mycolata like *Corynebacterium glutamicum*[25]. These mutations identified in the Pks13 and PptT proteins, which are both required for the final condensation of MA, imply that the undisrupted MA organisation is crucial for M. amalyticus attachment.

The remaining three GAMs contained mutations at three different loci (Table 1). GAM5 had a mutation occurring upstream of the *acpM* gene, predicted to occur within the putative Shine-Delgarno ribosomal binding site, potentially abolishing its translation (Supplementary Fig. 3a). AcpM is an acyl carrier protein involved in production of the meromycoloyl-AMP product of the FAS II pathway[20,26], one of two fatty acids condensed by Pks13 (See discussion). Mutations identified in GAM2 and GAM3 were located in two different loci, a disruptive in-frame deletion within *iolJ* and a SNP upstream of the *iolT* gene, encoding an aldolase and transfer protein, respectively, involved in myo-inositol biosynthesis (Supplementary Fig. 3b, c)[27,28]. The upstream mutation in GAM3 is predicted to occur within the putative promotor sequence of the *iolT* gene (Supplementary Fig. 3c). Mutations detected in non-coding regions appear to impact expression of genes involved in MA biosynthesis. Whole genome sequence data of all eleven GAMs revealed different mutations impacting gene products associated with different pathways that all contribute the synthesis of MA (Fig. 3e).

G. amarae resistance to M. amalyticus infection occurs through loss of MA outer layer

Genomic analysis suggested disruptions in the MA biosynthesis pathway rendered *G. amarae* resistant to M. amalyticus infection. We used cryoET to investigate the structural implications of these

https://doi.org/10.1038/s41467-025-56933-4

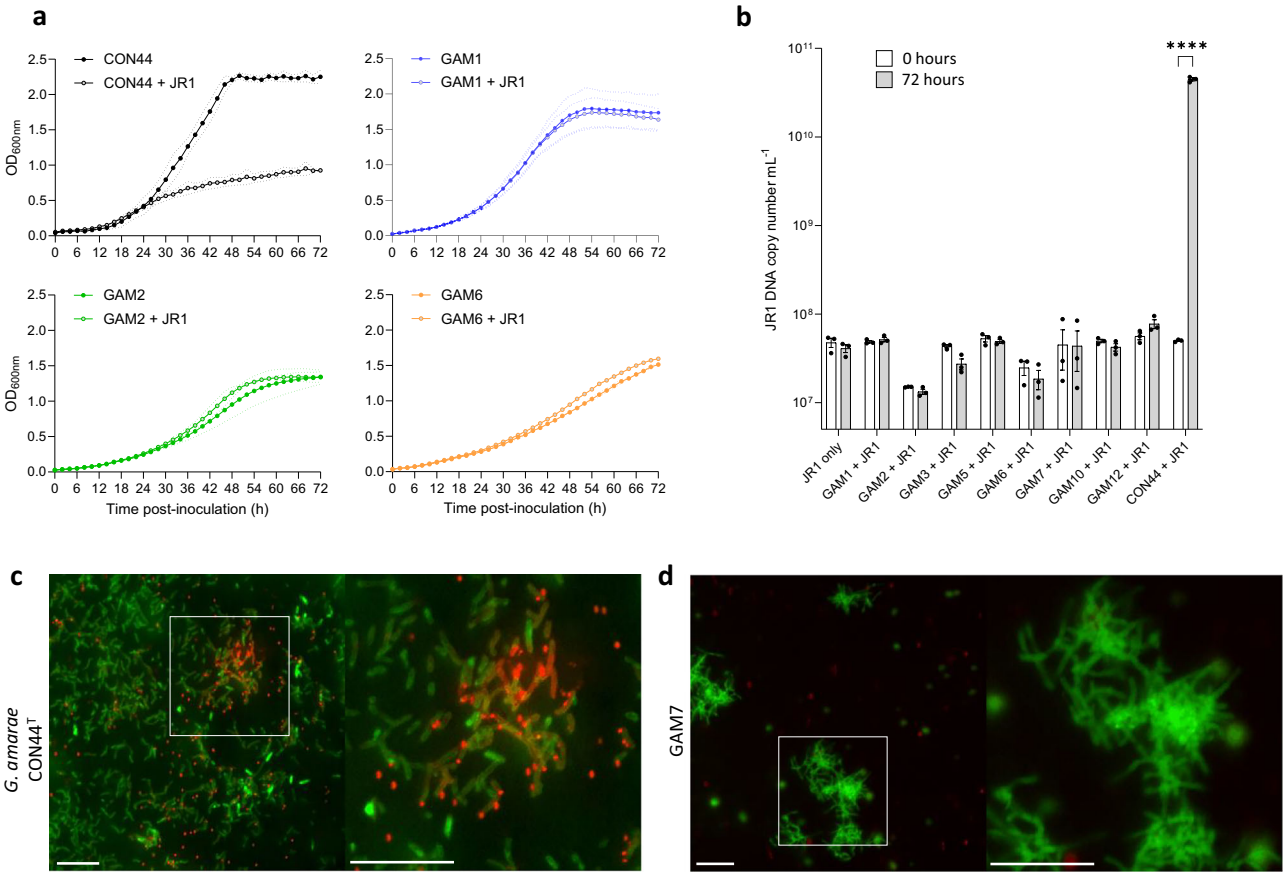

Fig. 2 | Growth kinetics and fluorescent microscopy of M. amalyticus and GAMs. a Growth curve of *G. amarae* CON44^T, GAM1, GAM2 and GAM6 in monoculture and coculture with M. amalyticus (MOI = 1.0) over 72 h. All GAMs exhibited lower final OD_{600} in comparison to the WT. As expected, growth in WT cocultures were heavily impaired, however each GAM tested displayed no reduction in growth when cocultured. **b** Direct dPCR measuring starting and final DNA copy number mL^{-1} of M. amalyticus in coculture. Abundance of M. amalyticus in GAM coculture was comparable to M. amalyticus monoculture. As expected, the copy number of M. amalyticus in *G. amarae* CON44^T coculture displayed statistically significant increase in abundance (two-way ANOVA Šídák's multiple comparisons test, $P < 0.0001$). Black circles represent each data point (error bars representing standard error of the mean, $n = 3$ biological replicates) with white and grey bars representing starting (0 h) and end point (72 h) respectively. **c** Fluorescent microscopy of membrane-stained *G. amarae* CON44^T-M. amalyticus coculture **d** and GAM7- M. amalyticus coculture, showing host and M. amalyticus cells in green and red, respectively. The white boxes represent the area shown in the zoomed micrographs to the right of each image. Due to reluctant uptake of membrane dye in GAM7, fluorescent excitation of *G. amarae* CON44^T and GAM7 were 488 nm and 408 nm wavelengths, respectively. Images were captured every three seconds using a Nikon T*i*E inverted fluorescence microscope. Original magnification is 60x with scale bar representing 20 µm (see supplementary movies 2 and 3 for more detail). These results were independently reproduced three times.

Table 1 | Mutations identified in each GAM when compared to the *G. amarae* WT (Accession number: CP045810)

Strain	Mutation	AA position	Gene	Product	Protein domain
Locus 1					
GAM6	Deletion (disruptive inframe deletion)	1765	*pks13*	Acyltransferase	Thioesterase domain (TE)
GAM7	SNP (missense) Gly > Cys	1606	*pks13*	Acyltransferase	Thioesterase domain (TE)
GAM10	SNP (missense) Cys > Trp	303	*pks13*	Acyltransferase	Ketosynthase domain (KS)
GAM11	SNP (missense) Trp > Ser	1755	*pks13*	Acyltransferase	Thioesterase domain (TE)
GAM12	SNP (missense) Pro > Gln	280	*aftB*	Arabinofuranosyltransferase	-
Locus 2					
GAM1	SNP (missense) Ala > Glu	53	*pptT*	4′-phosphopantetheinyl transferase (PPTase)	-
GAM4	Deletion (frameshift) Val > fs	122	*pptT*	4′-phosphopantetheinyl transferase (PPTase)	-
GAM9	SNP (stop gained) Ser > STOP	195	*pptT*	4′-phosphopantetheinyl transferase (PPTase)	-
Locus 3					
GAM5	SNP G > C	-	*acpM*	Acyl carrier protein	Putative Shine-Dalgarno sequence
Locus 4					
GAM2	Deletion (disruptive inframe deletion)	40	*iolJ*	Myo-inositol aldolase	-
Locus 5					
GAM3	SNP T > G	-	*iolT*	Myo-inositol transporter	Putative promoter sequence

https://doi.org/10.1038/s41467-025-56933-4

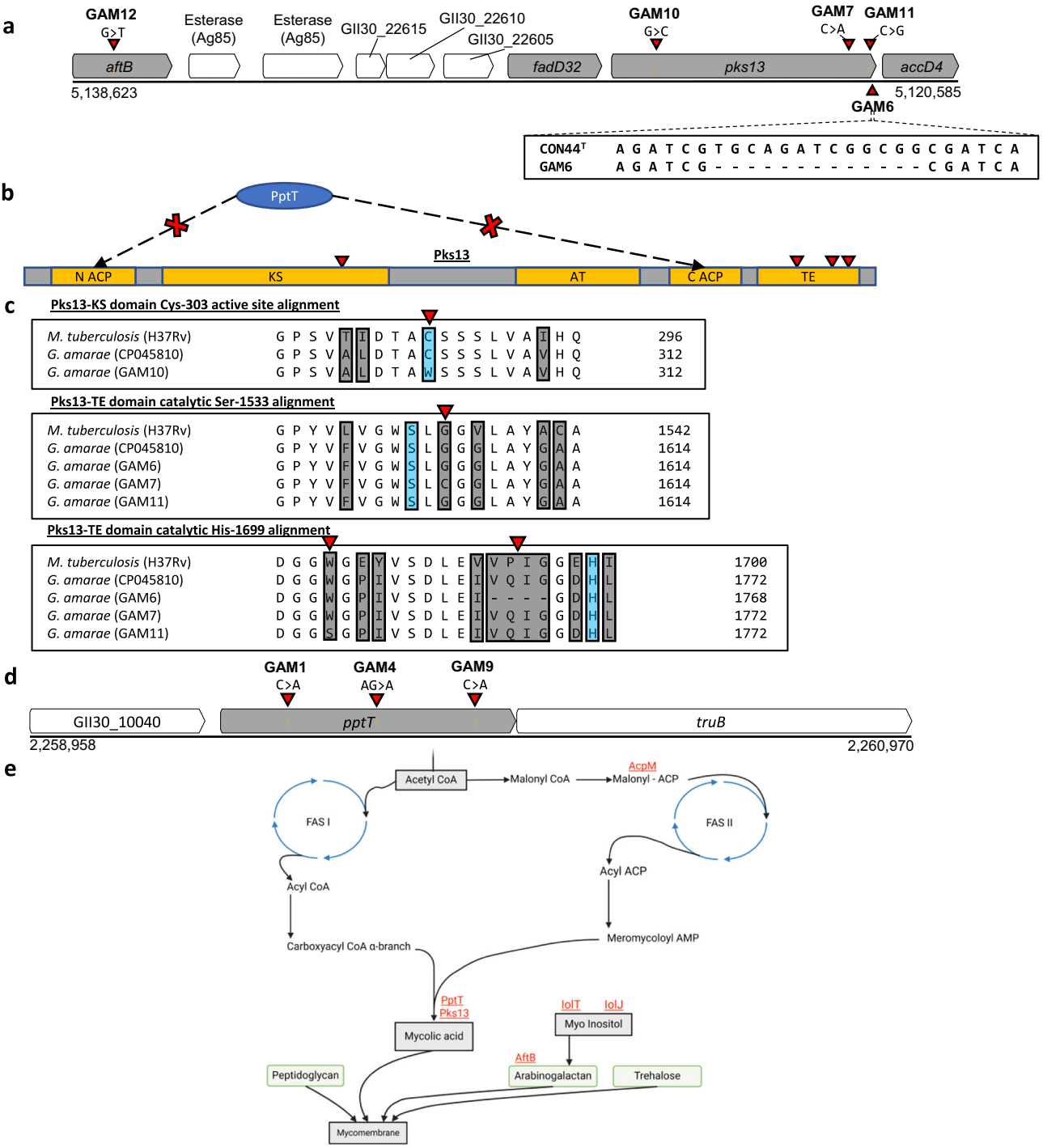

mutations. Wild type and GAM mutants 1–3 and 6 were incubated with M. amalyticus and imaged by cryo transmission electron microscopy (cryoTEM). We searched each grid for interactions between M. amalyticus and GAM cells using low magnification cryoTEM and acquired a tilt series at regions of interest. As previously described[10], *G. amarae* CON44^T was frequently found with multiple M. amalyticus cells attached (Fig. 4a). However, parasite attachment in each of the four GAMs was rare (Supplementary Fig. 1), with further cryoET imaging revealing a relatively large (>50 nm) gap between the boundaries of the two cells in those occasional instances (Fig. 4a). We also noticed a substantial change in appearance of the GAM membranes. While *G. amarae* CON44^T had a well-defined cytoplasmic membrane and MA outer layer, the MA layer in the GAMs was indistinct with poor definition. Sub-tomogram averaging and density-profile analysis were then used to compare the differences in the cellular envelope of each strain (Fig. 4b, c). Density-profile analysis showed that wildtype had four distinct densities, one each for the cytoplasmic membrane, peptidoglycan layer, AG and MA outer layers (Fig. 4b). However, each GAM strain lacked a distinct density for their MA outer membrane layer, with GAM2 and GAM3 seemingly lacking an associated AG trough. Sub-tomogram averaging was performed by selecting sub-volumes along the cell membrane and aligned/averaged by particle estimation for electron tomography (PEET) as described previously[29,30]. Representative slices through each 3D sub-tomogram average are shown as orthogonal planes (Fig. 4c). While the MA outer layer was clearly resolved in the *G. amarae* CON44^T average, no such clarity was seen in those derived from GAMs (Fig. 4c). An average did converge for the cytoplasmic

Fig. 3 | Genomic loci of mutations within mycolic acid biosynthetic pathway. **a** Mutations in GAM6, GAM7, GAM10, GAM11 and GAM12 are shown in the first locus by a red triangle and SNPs indicated above. GAM12 contains a missense mutation in the predicted *aftB* gene. The remaining mutations all occur in different locations in *pks13*. Genes shaded in grey are predicted to encode proteins involved in AG and MA biosynthesis pathways. **b** Schematic of Pks13 protein, orange segments indicate the catalytic N-terminal acyl carrier proteins (ACP), ketoacyl synthase (KS), acyl transferase (AT), C-terminal ACP and thioesterase (TE) domains[49]. Red triangles indicate the location of the mutations in GAM6, GAM7, GAM10 and GAM11. Blue oval represents PptT protein priming the Pks13 N-terminal and C-terminal ACP domains with 4′-phosphopantetheinyl (P-pant) arm[49]. Mutations acquired in GAM1, GAM4 and GAM9 within PptT likely result in protein dysfunction (indicated by the red Xs). **c** Amino acid alignments comparing the conserved KS and TE catalytic domains of each GAM with the *G. amarae* CON44^T (Accession number: CP045810), and *M. tuberculosis* H37Rv (Accession number: NC_000962.3)[49]. Catalytic residues identified in *M. tuberculosis*[49], are highlighted in blue, with red triangles indicating the positions of amino acid substitutions/deletions. Residue discrepancies are highlighted in grey. In GAM10 the predicted catalytic cysteine (Cys-303) is substituted with tryptophan (Try-303). In the GAM7 TE domain, a cysteine substitution of glycine (Gly-1606) occurred two residues downstream of the predicted catalytic serine (Ser-1606, Ser-1533 in *M. tuberculosis*). Further downstream within the TE domain GAM11 and GAM6 encode a Ser-1755 substitution and Val-1765-Gln-Ile-Gly-1768 deletions respectively. **d** GAM1, GAM4 and GAM9 share mutations within the *pptT* gene, with red triangles indicating the corresponding mutations above. **e** Basic overall mycolic acid biosynthetic pathway. Multiple proteins are involved in the coordination of the final condensation of MA, a complex process that requires several precursor reactions[20,49]. Pks13 condensase requires PptT posttranslational priming and works in concert with various acyl carrier proteins to catalyse the biosynthesis of MA, by condensing the FAS I and FAS II cycle outputs[20,50]. In combination with peptidoglycan, trehalose and arabinogalactan (outputs in green boxes), MA forms the mycomembrane. Red text highlight gene mutations identified in each GAM. Created in BioRender. Rose, J. (2025) http://BioRender.com/o17z397.

membranes and peptidoglycan layers in each GAM, indicating that both layers are intact in the mutant strains. Together these data indicate that in all four GAMs, the structural organisation and hence function of their outer membranes had been modified substantially, and in some cases lost entirely.

Finally, we considered how these structural perturbations might affect the hydrophobicity of the mutant strains. As mentioned earlier, *G. amarae* CON44^T strains are highly hydrophobic because of their outer MA layer, a feature which allows them to stabilise foams on activated sludge plants, with associated operating problems[31,32]. The simple MATH assay of Rosenberg et al.[33] showed a much lower hydrophobic reading in the *G. amarae* mutants compared to the wild type *G. amarae* CON44^T (Fig. 4d). Since cellular hydrophobicity of Mycolata reflects the presence of MA, these trends provide further evidence for MA disruption/absence.

Discussion

There is much still to be learned about the host-parasite relationships involving members of the Patescibacteria. These bacteria are ubiquitous in the environment and especially abundant in WWTPs[5,6,14]. The current literature suggests that considerable diversity exists in the life cycle of these organisms[34–36]. This study aimed to elucidate the mechanistic details of infection processes of M. amalyticus, a necrotrophic obligate parasite of its host *G. amarae*. How these organisms are attracted to their host populations and the mechanisms responsible for the subsequent lysis was unknown. Such information is important since these Patescibacteria, by their selective action may impact on the community composition of WWTPs and hence their performance[5,6,11]. Multiple techniques have been employed to understand how these parasites interact with their host cells[7,8,10,37,38]. Our study utilised cryoET in conjunction with lab-based evolution and WGS to investigate the interaction of M. amalyticus with its prey *G. amarae*.

Evidence presented here indicates that M. amalyticus attraction and attachment to *G. amarae* is not a random event but is facilitated by type IV pili. We noted multiple pili forming connections between M. amalyticus and *G. amarae* cells, in a similar manner reported in the episymbiotic relationship of Saccharibacteria TM7i and its bacterial host *Leucobacter aridicollis*[8]. Inhibition of type IV pili extrusion supressed the characteristic twitching motility and consequently inhibited TM7i host attachment. Whether the host-parasite interaction between M. amalyticus and *G. amarae* involves a similar motility process is unknown.

CryoET used here captured the interaction of parasite and host cells at nanometre resolution, enabling identification a tube-like structure connecting associating cells. Similar structures have been documented in other microbial symbiotic and pathological relationships[39], but its function is still unclear. Imaging also revealed two previously unknown anatomical features on and within M. amalyticus cells. A lance-like appendage comprising a tube structure with a barbed density on the extracellular tip was seen protruding from M. amalyticus, and the other, complex membrane compartments forming at the poles. These features were only seen when the parasitic interaction had occurred or after exposure to spent media from *G. amarae* cultures. The latter suggests that they are induced by exocellular host cell products, and not necessarily directly associated with parasitic contact. A comparison of the lance-like and tube-like structures suggests they may be the same complex at different stages of infection, implying a phase-dependent, multifunctional role. The polar intracellular compartments have not been previously described, and their role in the parasitic process is unknown, although similar structures were captured in CryoET of TM7x during infection of its host[38].

Although speculative, we propose here a model of parasite infection consistent with findings from other Saccharibacteria studies[8,9], whereby M. amalyticus type IV pili are essential for surface recognition and attachment to the *G. amarae* host. During this recognition phase the pili anchors to the MA structure. Following type IV pili attachment and retraction, penetration of the host cell using the lance/conduit tube-like structures may facilitate the transfer of cargo and nutrients across the intimate transmembrane junction formed between the parasite and host cells. Recent investigation into two genes encoded within M. amalyticus was demonstrated to encode enzymes with catalytic activity involved in the breakdown of AG[40]. The resulting metabolites generated by AG breakdown may serve as an essential source of nutrients for M. amalyticus growth. This may suggest that the MA provides a site for M. amalyticus attachment to enable access to AG for parasitic feeding. This mode of parasitism is unique to M. amalyticus and there is no indication that other epibiotic parasites such as *Vampirococcus*[41] and *Bdellovibrio*[42] depend on mycolic acids for their attachment.

We provide a clear demonstration that the MA outer layer plays an essential role in M. amalyticus infection of *G. amarae*, through several experimental methods, including genome sequencing, morphological surveillance and biochemical experimentation. Together, the data generated indicates that only when the host MA layer is intact can M. amalyticus initiate infection and induce host cell lysis. Eight out of eleven GAMs exhibited mutations impacting expression of proteins directly involved in the maturation of MA, these proteins were Pks13, PptT and AcpM[20]. Given the nature and location of the mutations identified in the GAMs, it is likely that the resulting tertiary structure and function of these proteins has been impaired. The results generated in this study show differences in the cellular capsule thickness and loss of surface hydrophobicity in GAMs, suggesting the absence of MA. This observation was noted in previous work by Hoffmann, et al.[43], describing an observable loss in cellular thickness of *C. glutamicum*

https://doi.org/10.1038/s41467-025-56933-4

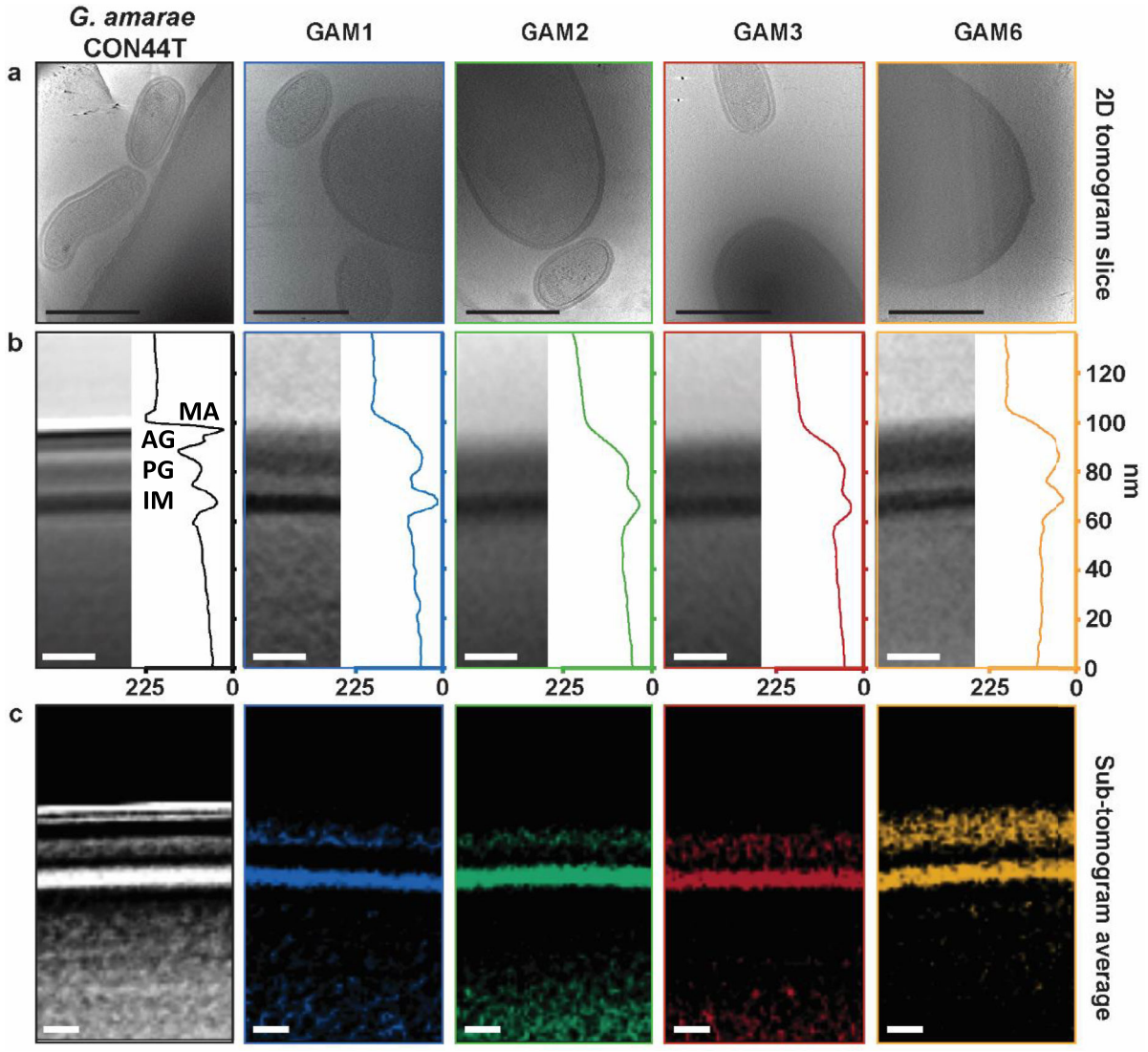

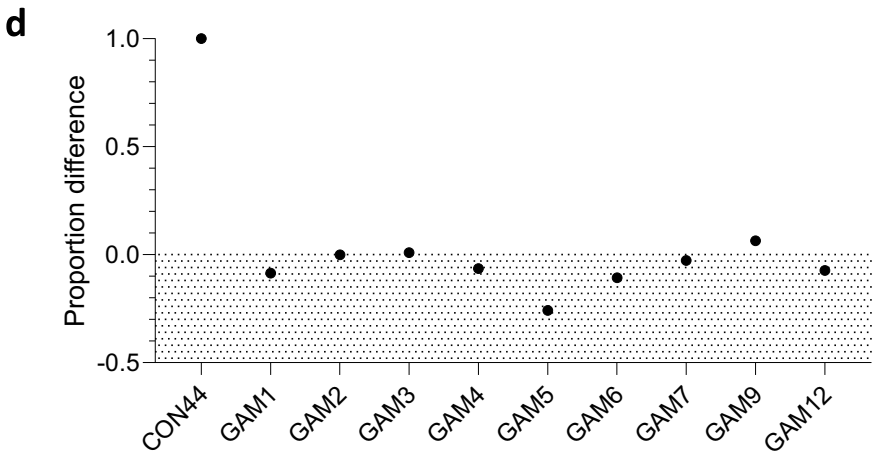

Δ*pks13* knockout mutants, when compared to the WT counterparts. The *C. glutamicum* Δ*pks13* mutants used in that study and earlier work[19] were MA deficient, displaying obvious loss in a distinct outer cellular layer, comparable to the tomograms generated here (Fig. 4b, c).

The remaining three GAMs appeared to have mutations within or preceding the AG biosynthetic pathways, with mutations in IolJ, IolT and AftB. IolJ and IolT are an aldolase and transfer protein respectively, involved in the myo-inositol metabolism[27,28], a precursor molecule for AG derivatives[44]. Myo-inositol is a component of larger molecules like phosphatidyl-myo-inositol, mannosyl-phosphatidyl-myo-inositol, phosphatidyl-myo-inositol mannosides, providing the structural components for the formation of the AG portion of the cell wall (Fig. 5)[44–46]. We believe that the mutations observed in these genes, namely GAM2 and GAM3, have led to an observable absence of where

Fig. 4 | CryoET analysis of GAM strains and hydrophobicity analysis of mycolic acid. a Example tomograms of *G. amarae* CON44^T and GAMs interacting with M. analyticus. Images are 2D slices (thickness = 10) through 3D reconstructed tomograms. *G. amarae* CON44^T and GAM cells, which are >500 nm in size, are clearly distinguishable from much smaller M. analyticus cells. **b** Profile analysis of the membrane envelopes of each strain, an average density of each membrane is shown in the left of each panel, with the profile analysis of this density shown on the right, with grey scale (225-0) on the x-axis, and distance on the y-axis. The *G. amarae* cell inner membrane, peptidoglycan, arabinogalactan and mycolic acid layers are labelled in left panel as IM, PG, AG and MA respectively. **c** Orthogonal views sub-tomogram averages of membrane envelopes of each strain, the density of each component (cytoplasm, cytoplasmic membrane, peptidoglycan layer, arabinogalactan and mycolic acid outer membrane) are shown against a black background. Scale bars represent 500 nm (**a**), 20 nm (**b**), and 10 nm (**c**). **d** MATH assay of *G. amarae* CON44^T and GAM cells. The y-axis represents the *G. amarae* CON44^T normalised difference in OD_{600} after incubation with hexadecane as outlined in the materials and methods ($n = 3$ biological replicates).

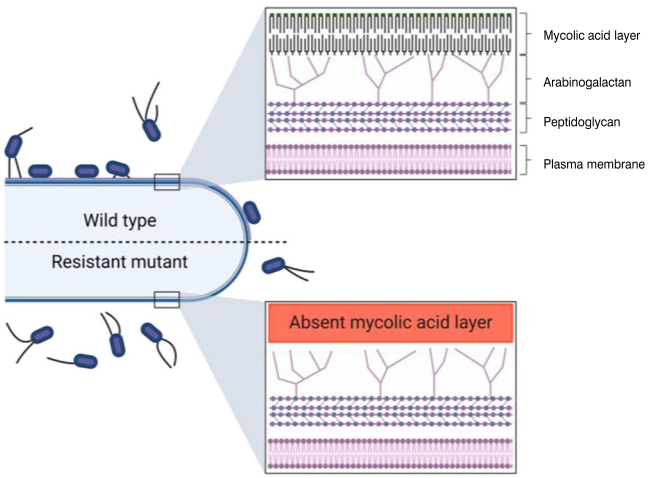

Fig. 5 | Summary figure depicting the model of M. amalyticus resistance. Mutations observed in genes detected in this study result in absent mycolic acid layer in myco-membrane, preventing attachment of M. amalyticus to the surface of GAMs, and subsequent lysis. Created in BioRender, Rose, J. (2025) http://BioRender.com/y60g982.

we would expect to see AG in Fig. 4b. However, this requires further investigation to confirm this hypothesis. The final mutant GAM12 contains a mutation within *aftB*. AftB is involved in the endpoint synthesis of AG therefore hypothesised to impact the linkage of AG and MA[21]. Using *C. glutamicum* Δ*aftB* knockout mutants, *aftB* deletion resulted in a reduction of MA tethered to the AG sub-layer[21]. In this study we observed similar results, likely reflecting a loss of MA attachment to AG in the case of GAM12. These data together with preexisting literature confirms that the surface receptor, or molecular target of M. amalyticus is likely MA.

The over proliferation of hydrophobic Mycolata in WWTPs results globally in the serious operational problem of stabilised surface foams, conceiving an environmentally friendly control strategy has attracted much interest. One shortcoming with using biological based control strategies is that their target bacteria tend to develop resistance. What this study shows is that mutations in these Mycolata select for populations with impaired growth and appear to be favoured in the genes encoding MA biosynthesis, with subsequent loss of hydrophobicity and thus loss of their ability to stabilise foams. Data presented here provides evidence that prolonged exposure to M. amalyticus will not inevitably lead to M. amalyticus-resistant Mycolata mutants capable of WWTP foam stabilisation. Complete eradication of Mycolata is neither feasible nor desirable, but if M. amalyticus can maintain Mycolata abundances below their foaming threshold, then control may be possible, however, this will have to be verified in-situ.

Further work will be directed at identifying host-parasitic system, especially in identifying the function and importance of the several previously unrecorded structures revealed by CryoET and seen only in M. amalyticus cells parasitising *G. amarae*. Future investigation of these structures will open new avenues to explore intriguing cell biology of the 'microbial dark matter' and M. amalyticus-like organisms, further demonstrating their complex life cycles and parasitism.

Methods

Bacterial strains, media and growth conditions

All strains grown as monoculture were incubated either in PYCa broth (5 g L^{-1} peptone, 3 g L^{-1} yeast extract, 1 g L^{-1} calcium chloride and 1 g L^{-1} glucose) or on solidified PYCa agar plates (12 g L^{-1} agar) at 28 °C for 48–120 h. M. amalyticus was co-cultured on CON44^T lawns, using 300 μL M. amalyticus 0.45 μm filtrate and harvested using PYCa and a sterile glass rod. As previously described[10], liquid co-cultures with each strain were seeded at an OD_{600} of 0.05 (≈3×10^6 CFU mL^{-1}) measured using a Novaspec III+ Spectrophotometer (Biochrom).

Gordonia amarae mutant generation

To generate and select for GAMs, long term co-cultures of M. amalyticus and *G. amarae* CON44 (wild type) were incubated for 48 h (one passage) as described previously[10] for a total of three passages. Each passage was seeded with an MOI of 1 and an OD_{600} of 0.05 in a total volume of 2 mL. At the conclusion of the third passage, 10 μL of co-culture was incubated on PYCa agar at 28 °C for 48–120 h, and single colonies purified. Once purified, M. amalyticus was spotted onto the lawns of each mutant to test for M. amalyticus resistance. After three rounds of testing M. amalyticus resistance, strains were then used for downstream applications.

CryoET sample preparation and data acquisition

Samples were prepared for vitrification by resuspending a loop of *G. amarae* and GAM culture scrapped from a plate in a liquid culture of M. amalyticus and incubated at 37 °C for 15 min. Immediately before vitrification, the resuspension was mixed with 10 nm colloidal gold beads precoated with 1% BSA (Sigma-Aldrich, Australia). The mixture was applied to glow-discharged copper Quantifoil holey extra thick carbon grids R2/2 (Quantifoil Micro Tools GmbH, Jena, Germany), blotted for 6–8 s, with a blot force of 8, at 37 °C, 100% humidity and plunged into liquid ethane using a Vitrobot Mark IV, FEI (Thermo Fisher Scientific). Micrographs of M. amalyticus-GAM interactions were acquired using an FEI Titan Krios G4, 300 keV FEG transmission electron microscope (Thermo Fisher Scientific), equipped with a BioQuantum K3 Imaging Filter (slit width 20 eV), and a K3 direct electron detector (Gatan) at a pixel size of 3.39 Å. Tilt series were collected automatically using Tomography 5 (Thermo Fisher Scientific) from −51° to +51° at 2° intervals with a defocus of −8 μm and a total electron fluence of 120 e-/Å^2.

Tomogram reconstruction

3D tomograms were generated using IMOD (Version 4.11.5), raw mrc 4 K images (3.39 Å/pix) were binned to 2 K (6.78 Å/pix), tilt images and poor-quality images were removed through visual inspection, and the remaining images were aligned using cross-correlation and fiducial tracking. Aligned tilt series were reconstructed into 3D tomograms by SIRT reconstruction using Tomo3D (version 2.2). Subsequent tomograms were then binned again to 1 K (13.56 Å/pix) for downstream analysis and segmentation. Representative 2D slice

images through 3D tomograms were produced using IMOD slicer window.

Tomogram segmentation and visualisation/ 3D-segmentation

Tomograms were pre-processed using Tomosim, segmentation of tomograms was done using the Dragonfly software (https://www.theobjects.com/dragonfly/index.html). Tomograms were processed using built-in filters, including histogram equalisation, Gaussian, and unsharp filters. Neural network 5-class U-Net (with 2.5D input of 5 slices) were trained on tomogram slices to recognise M. amalyticus cytoplasmic membrane, outer layer, and pili, and *G. amarae* cytoplasmic membrane and outer mycolic acid layer. Lance densities were manually curated due to their low abundance. All segmented features were further fine-tuned to achieve high-quality automated 3D segmentation. 2D images and 3D movies were created using the software's built-in tools image and movie production.

Tomogram data analysis

Measurements were made using IMOD (Version 4.11.5). For the diameter of tube-like structures and lance-like structures, measurements were taken from the centre of each density across the lumen. Length measurements of tube-like and lance-like structures were measured along the longest continuous density. Finally, pili were measured across the width of the density. An average and standard deviation was calculated from five independent measurements.

Fluorescence live cell microscopy

Following 48 h incubation, *G. amarae* CON44^T and GAM cells were stained with 1X CellMask™ green plasma membrane stain (Invitrogen™). Cells were incubated at 37 °C for 30 min with shaking, and then centrifuged at 16,000 × *g* for 2 min, and resuspended in PYCa. Centrifugation and resuspension were repeated once more. Similarly, M. amalyticus cells were stained with 1X CellMask™ deep red plasma membrane stain (Invitrogen™) and incubated at 37 °C for 30 min with shaking, however the centrifugation steps were performed at 21,380 × *g* for 15 min. Using 5 µL of each strain, we spotted onto a glass slide and coverslip and imaged using an eclipse Ti light microscope (Nikon) at 60x with oil. Images of *G. amarae* CON44^T and GAM7 were captured with cells excited with 488 nm and 408 nm wavelengths, respectively. Difference in wavelength used for cell excitation was due to reluctant uptake of membrane dye in GAM7.

Coculture growth experiments

Growth curve experiments were conducted similarly to as previously described in ref. 10. Briefly, using two biological replicates and in technical duplicates, 2 mL co-cultures were incubated for 72 h in 12-well cell culture plates (Greiner) and seeded with an MOI of 1. Cultures were grown and measured using the CLARIOstar plate reader platform (BMB Labtech) with 28 °C incubation and shaking at 100 RPM (meander corner well shaking) over 72 h. Every 2 h the OD_{600} of wells was measured using a well-scan matrix (5 × 5, 10 flashes per well) with shaking increased to 200 RPM for 2 min prior to measurement.

M. amalyticus in spent CON44^T media

CON44^T cultured in 10 mL broth was centrifuged at 3000 × *g* for five minutes and filtered with a 0.45 µm filter, with the filtrate retained. 500 µL of M. amalyticus (10^9 pfu/mL) was then centrifuged at 21,380 × *g* for 1 h, with the pellet resuspended in 500 µL of the spent CON44^T media filtrate.

Direct dPCR of M. amalyticus in liquid coculture

To measure growth of M. amalyticus in coculture, starting (0 h) and endpoint (72 h) samples were taken, and prepared as described[10]. Briefly, samples were thawed at room temperature prior to two minutes microwaving, immediately vortexed for five seconds, diluted 1/100 in Milli-Q water and left on ice. EvaGreen® (QIAGEN) master mix (12 µl reactions) were prepared as per the manufacturer's instructions using 5 µl sample, forward and reverse primers at a final concentration of 400 nM each, and EcoRI-HF (NEB) at a final concentration of 20 U µL^{-1}. Amplifying a 167 bp target, the forward primer 5′-GTTGGTAGTGCTCGCTGCAT-3′ and reverse primer 5′-TCACCCGCCTCGTATTGACT -3′, were used to measure M. amalyticus abundance. In three biological replicates, digital PCR was performed using QIAcuity Nanoplates 8.5 k (QIAGEN) on the QIAcuity (QIAGEN). The conditions used were as followed: 2 min initial heat activation at 95 °C, 40 cycles of 3-step cycling including denaturation at 95 °C for 15 s, annealing at 60 °C for 15 s, extension at 72 °C for 15 s, followed by cooling at 40 °C for 5 min. Imaging was captured with 150 ms exposure duration and default gain of 6. All samples were normalised to a common threshold of 45.

Whole genome sequencing and SNP analysis

Genomic DNA from 10 mL log-phase of each strain was extracted using the DNeasy soil kit (Qiagen) with 10-min bead beating on a Vortex Genie 2 fitted with a 24-tube vortex adapter, according to the manufacturer's instructions. For Illumina sequencing genomic DNA (150 ng) was prepared using the NEBNext Ultra II DNA library prep kit (NEB) and whole genome sequenced on an Illumina MiSeq v2 300-cycle kit (Illumina). Reads were filtered using Trimmomatic v0.36.6 with default settings (Q scores of ≥20). SNP analysis was performed with snippy v4.6.0 using default settings (minimum coverage ≥10) and compared to the Genbank *G. amarae* reference sequence (Accession no.: CP045810). Mutations identified in GAMs were then crosschecked against the parent lab strain (WT) with shared mutations removed from the analysis. This ensured that all mutations identified persisted as a result of selective pressure imposed by M. amalyticus, helping discriminate between spontaneous mutations generating resistance to M. amalyticus and other random mutations. In addition, any identical mutations shared between GAMs were also excluded. The remaining unique mutations were then investigated and visualised using Geneious Prime v2023.0.4 (Biomatters). Promotech v1.0 analysis was used to identify predicted promoter sequences using whole genome mode and the RF-HOT model with default settings: --threshold 0.5[47]. Shine Find (Galaxy Version 21.1.0.0) was used to identify predicted Shine-Dalgarno sequences with default settings: --lookahead_min = 3; --lookahead_max = 17; --top_only = 1[48]. Mutations occurring in none coding regions were then crosschecked for occurrences in these predicted promoter regions and ribosomal binding sites. Genes of interest or with no predicted function were compared to the NCBI BLASTp data base and the UniProt database. Raw sequence data have been deposited under BioProject Accession Number PRJNA1194146.

Sub-tomogram averaging

Sub-tomogram averaging (STA) was done using PEET software package (IMOD Version 4.11.5). Tomograms were processed by SIRT reconstruction and binned to (13.56 Å/pix), 150-200 particles were picked along the cytoplasmic membrane of the cell with xyz box dimensions of 60, 100, 60 voxels respectively. Manual alignment was done during picking, with the cytoplasmic membrane along the x-axis intersecting the centre of the y-axis. The cytoplasmic membrane was chosen as it was the only consistent density observed in all samples. Particle co-ordinates were used for three rounds of restricted alignment in PEET. STA were depicted using chimeraX software.

Microbial adhesion to hydrocarbon (MATH) assay

To assess the hydrophobicity of strains, the microbial adhesion to hydrocarbon (MATH) assay was conducted using n-hexadecane, based

on methods previously described[31,33]. Into 1.5 mL microcentrifuge tubes, 100 μL of n-hexadecane was added to 1.1 mL of each strain and vortexed for 10 s, then left to sit for 15 min. The proportion similarity was calculated by measuring the OD_{600} of each strain before and after hexadecane treatment. Each strain was measured in three biological replicates.

Statistics and reproducibility

Experiments were statistically analysed using a two-way ANOVA. All statistical analysis was performed using GraphPad Prism v10.2.3, with some figures generated using Biorender. Experiments were performed in biological triplicates unless otherwise stated. All image results were obtained from at least three independent reproducible images.

Reporting summary

Further information on research design is available in the Nature Portfolio Reporting Summary linked to this article.

Data availability

The raw DNA sequence data generated in this study have been deposited in GenBank under BioProject Accession Number PRJNA1194146. All additional data are available within this article and Supplementary data.

References

1. Seviour, B. & Nielsen, P. *Microbial Ecology of Activated Sludge Preface* (IWA Publishing, 2010).
2. Nielsen, P. H., Saunders, A. M., Hansen, A. A., Larsen, P. & Nielsen, J. L. Microbial communities involved in enhanced biological phosphorus removal from wastewater-a model system in environmental biotechnology. *Curr. Opin. Biotechnol.* **23**, 452–459 (2012).
3. Hu, H. et al. Global abundance patterns, diversity, and ecology of Patescibacteria in wastewater treatment plants. *Microbiome* **12**, 55 (2024).
4. Fujii, N. et al. Metabolic potential of the superphylum Patescibacteria reconstructed from activated sludge samples from a municipal wastewater treatment plant. *Microbes Environ.* **37**, ME22012 (2022).
5. Albertsen, M. et al. Genome sequences of rare, uncultured bacteria obtained by differential coverage binning of multiple metagenomes. *Nat. Biotechnol.* **31**, 533–538 (2013).
6. Marcy, Y. et al. Dissecting biological "dark matter" with single-cell genetic analysis of rare and uncultivated TM7 microbes from the human mouth. *Proc. Natl Acad. Sci. USA* **104**, 11889–11894 (2007).
7. He, X. et al. Cultivation of a human-associated TM7 phylotype reveals a reduced genome and epibiotic parasitic lifestyle. *Proc. Natl Acad. Sci.* **112**, 244–249 (2015).
8. Xie, B. et al. Type IV pili trigger episymbiotic association of Saccharibacteria with its bacterial host. *Proc. Natl Acad. Sci. USA* **119**, e2215990119 (2022).
9. Wang, Y. et al. Genetic manipulation of Patescibacteria provides mechanistic insights into microbial dark matter and the epibiotic lifestyle. *Cell* **186**, 4803–4817.e4813 (2023).
10. Batinovic, S., Rose, J. J., Ratcliffe, J., Seviour, R. J. & Petrovski, S. Cocultivation of an ultrasmall environmental parasitic bacterium with lytic ability against bacteria associated with wastewater foams. *Nat. Microbiol.* **6**, 703–711 (2021).
11. Parks, D. H. et al. A standardized bacterial taxonomy based on genome phylogeny substantially revises the tree of life. *Nat. Biotechnol.* **36**, 996–1004 (2018).
12. Rheims, H., Rainey, F. & Stackebrandt, E. A molecular approach to search for diversity among bacteria in the environment. *J. Ind. Microbiol.* **17**, 159–169 (1996).
13. Vigneron, A., Cruaud, P., Guyoneaud, R. & Goñi-Urriza, M. Into the darkness of the microbial dark matter in situ activities through expression profiles of Patescibacteria populations. *Front. Microbiol.* **13**, 1073483 (2023).
14. Kuroda, K. et al. Metabolic implications for predatory and parasitic bacterial lineages in activated sludge wastewater treatment systems. *Water Res. X* **20**, 100196 (2023).
15. Sartori-Rupp, A. et al. Correlative cryo-electron microscopy reveals the structure of TNTs in neuronal cells. *Nat. Commun.* **10**, 342 (2019).
16. Gaisin, V. A., van Wolferen, M., Albers, S.-V. & Pilhofer, M. Distinct life cycle stages of an ectosymbiotic DPANN archaeon. *ISME J.* **18**, wrae076 (2024).
17. Johnson, M. D. et al. Large attachment organelle mediates interaction between *Nanobdellota* archaeon YN1 and its host. *ISME J.* **18**, wrae154 (2024).
18. Craig, L. et al. Type IV pilus structure by cryo-electron microscopy and crystallography: implications for pilus assembly and functions. *Mol. Cell* **23**, 651–662 (2006).
19. Portevin, D. et al. A polyketide synthase catalyzes the last condensation step of mycolic acid biosynthesis in mycobacteria and related organisms. *Proc. Natl Acad. Sci. USA* **101**, 314–319 (2004).
20. Marrakchi, H., Lanéelle, M.-A. & Daffé, M. Mycolic acids: structures, biosynthesis, and beyond. *Chem. Biol.* **21**, 67–85 (2014).
21. Seidel, M. et al. Identification of a novel arabinofuranosyltransferase AftB involved in a terminal step of cell wall arabinan biosynthesis in Corynebacterianeae, such as Corynebacterium glutamicum and Mycobacterium tuberculosis. *J. Biol. Chem.* **282**, 14729–14740 (2007).
22. Besra, G. S. et al. A new interpretation of the structure of the mycolyl-arabinogalactan complex of Mycobacterium tuberculosis as revealed through characterization of oligoglycosylalditol fragments by fast-atom bombardment mass spectrometry and 1H nuclear magnetic resonance spectroscopy. *Biochemistry* **34**, 4257–4266 (1995).
23. McNeil, M., Daffe, M. & Brennan, P. Location of the mycolyl ester substituents in the cell walls of mycobacteria. *J. Biol. Chem.* **266**, 13217–13223 (1991).
24. McNeil, M., Daffe, M. & Brennan, P. J. Evidence for the nature of the link between the arabinogalactan and peptidoglycan of mycobacterial cell walls. *J. Biol. Chem.* **265**, 18200–18206 (1990).
25. Chalut, C., Botella, L., de Sousa-D'Auria, C., Houssin, C. & Guilhot, C. The nonredundant roles of two 4'-phosphopantetheinyl transferases in vital processes of Mycobacteria. *Proc. Natl Acad. Sci. USA* **103**, 8511–8516 (2006).
26. Mdluli, K. et al. Inhibition of a Mycobacterium tuberculosis β-ketoacyl ACP synthase by isoniazid. *Science* **280**, 1607–1610 (1998).
27. Yoshida, K.-i et al. myo-Inositol catabolism in Bacillus subtilis. *J. Biol. Chem.* **283**, 10415–10424 (2008).
28. Yoshida, K.-I., Yamamoto, Y., Omae, K., Yamamoto, M. & Fujita, Y. Identification of two myo-inositol transporter genes of Bacillus subtilis. *J. Bacteriol.* **184**, 983–991 (2002).
29. Ghosal, D. et al. Molecular architecture, polar targeting and biogenesis of the Legionella Dot/Icm T4SS. *Nat. Microbiol.* **4**, 1173–1182 (2019).
30. Nicastro, D. et al. The molecular architecture of axonemes revealed by cryoelectron tomography. *Science* **313**, 944–948 (2006).
31. Petrovski, S. et al. An examination of the mechanisms for stable foam formation in activated sludge systems. *Water Res.* **45**, 2146–2154 (2011).
32. Petrovski, S., Batinovic, S., Rose, J. J. & Seviour, R. J. Biological control of problematic bacterial populations causing foaming in activated sludge wastewater treatment plants—phage

therapy and beyond. *Lett. Appl. Microbiol.* **75**, 776–784 (2022).
33. Rosenberg, M., Gutnick, D. & Rosenberg, E. Adherence of bacteria to hydrocarbons: a simple method for measuring cell-surface hydrophobicity. *FEMS Microbiol. Lett.* **9**, 29–33 (1980).
34. Bor, B. et al. Phenotypic and physiological characterization of the epibiotic interaction between TM7x and its basibiont Actinomyces. *Microb. Ecol.* **71**, 243–255 (2016).
35. Bedree, J. K. et al. Quorum sensing modulates the epibiotic-parasitic relationship between Actinomyces odontolyticus and its Saccharibacteria epibiont, a Nanosynbacter lyticus strain, TM7x. *Front. Microbiol.* **9**, 2049 (2018).
36. Fujii, N. et al. Unique episymbiotic relationship between Candidatus Patescibacteria and Zoogloea in activated sludge flocs at a municipal wastewater treatment plant. *Environ. Microbiol. Rep.* **16**, e70007 (2024).
37. Dong, P.-T. et al. Episymbiotic Saccharibacteria induce intracellular lipid droplet production in their host bacteria. *ISME J.* **18**, wrad034 (2024).
38. Zhong, Q. et al. Episymbiotic Saccharibacteria TM7x modulates the susceptibility of its host bacteria to phage infection and promotes their coexistence. *Proc. Natl Acad. Sci. USA* **121**, e2319790121 (2024).
39. Johnson, M. D. et al. Cell-to-cell interactions revealed by cryo-tomography of a DPANN co-culture system. *Nat. Commun.* **15**, 7066 (2024).
40. Al-Jourani, O. et al. Identification of D-arabinan-degrading enzymes in mycobacteria. *Nat. Commun.* **14**, 2233 (2023).
41. Moreira, D., Zivanovic, Y., López-Archilla, A. I., Iniesto, M. & López-García, P. Reductive evolution and unique predatory mode in the CPR bacterium Vampirococcus lugosii. *Nat. Commun.* **12**, 2454 (2021).
42. Sockett, R. E. Predatory lifestyle of Bdellovibrio bacteriovorus. *Annu. Rev. Microbiol.* **63**, 523–539 (2009).
43. Hoffmann, C., Leis, A., Niederweis, M., Plitzko, J. M. & Engelhardt, H. Disclosure of the mycobacterial outer membrane: cryo-electron tomography and vitreous sections reveal the lipid bilayer structure. *Proc. Natl Acad. Sci. USA* **105**, 3963–3967 (2008).
44. Sancho-Vaello, E., Albesa-Jové, D., Rodrigo-Unzueta, A. & Guerin, M. E. Structural basis of phosphatidyl-myo-inositol mannosides biosynthesis in mycobacteria. *Biochim. et Biophys. Acta (BBA)-Mol. Cell Biol. Lipids* **1862**, 1355–1367 (2017).
45. Gilleron, M., Nigou, J., Nicolle, D., Quesniaux, V. & Puzo, G. The acylation state of mycobacterial lipomannans modulates innate immunity response through toll-like receptor 2. *Chem. Biol.* **13**, 39–47 (2006).
46. Salman, M., Lonsdale, J. T., Besra, G. S. & Brennan, P. J. Phosphatidylinositol synthesis in mycobacteria. *Biochim. et Biophys. Acta (BBA)-Mole. Cell Biol. Lipids* **1436**, 437–450 (1999).
47. Chevez-Guardado, R. & Peña-Castillo, L. Promotech: a general tool for bacterial promoter recognition. *Genome Biol.* **22**, 1–16 (2021).
48. Ramsey, J. et al. Galaxy and Apollo as a biologist-friendly interface for high-quality cooperative phage genome annotation. *PLOS Comput. Biol.* **16**, e1008214 (2020).
49. Gavalda, S. et al. The Pks13/FadD32 crosstalk for the biosynthesis of mycolic acids in Mycobacterium tuberculosis. *J. Biol. Chem.* **284**, 19255–19264 (2009).
50. Pawełczyk, J. & Kremer, L. The molecular genetics of mycolic acid biosynthesis. *Microbiol. Spectrum* **2**, MGM2-0003-2013 (2014).

Acknowledgements

We thank Jay Laws for assistance with fluorescent microscopy and Matthew Swulius for help with tomographic data analysis using TomoSim. Cryo-EM data were collected at the Ian Holmes Imaging Centre, Bio21, University of Melbourne. J.J.A.R. was the awardee of a La Trobe University postgraduate award. This work was funded by university funds provided by the department to S.P. D.G. is supported by a Cumming Global Centre for Pandemic Therapeutics Foundation Grant, an HFSP grant (https://doi.org/10.52044/HFSP.RGEC332023.pc.gr.168585) and an NHMRC grant (APP1196924).

Author contributions

D.G. and S.P. conceived and designed the study. J.J.A.R generated all *G. amarae* mutants, performed whole genome sequence, and bioinformatic analysis with assistance from S.B. J.J.A.R performed all wet lab work including growth curves, dPCR, biochemical assays and fluorescent microscopy. M.D.J. performed all electron microscopy and tomogram analysis with the assistance of M.R. under the guidance of D.G. J.J.A.R., M.D.J. and S.P. wrote the manuscript in consultation with S.B., R.J.S. and D.G.

Competing interests

The authors declare no competing interests.

Additional information

Supplementary information The online version contains supplementary material available at https://doi.org/10.1038/s41467-025-56933-4.

Correspondence and requests for materials should be addressed to Debnath Ghosal or Steve Petrovski.

Peer review information *Nature Communications* thanks Xu Chen, Takashi Narihiro and the other, anonymous, reviewer(s) for their contribution to the peer review of this work. A peer review file is available.